Diffusioosmosis-driven dispersion of colloids: A Taylor dispersion analysis with experimental validation

Benjamin M. Alessio[1], Suin Shim[2], Ankur Gupta[3] and Howard A. Stone[2]†

[1]Department of Physics, Princeton University, Princeton, NJ 08544, USA

[2]Department of Mechanical and Aerospace Engineering, Princeton University, Princeton, NJ 08544, USA

[3]Department of Chemical and Biological Engineering, University of Colorado, Boulder, CO 80301, USA

(Received xx; revised xx; accepted xx)

Diffusiophoresis refers to the movement of colloidal particles in the presence of a concentration gradient of a solute and enables directed motion of colloidal particles in geometries that are inaccessible, such as dead-end pores, without imposing an external field. Previous experimental reports on dead-end pore geometries show that even in the absence of mean flow, colloidal particles moving through diffusiophoresis exhibit significant dispersion. Existing models of diffusiophoresis are not able to predict the dispersion and thus the comparison between the experiments and the models is largely qualitative. To address these quantitative differences between the experiments and models, we derive an effective one-dimensional equation, similar to a Taylor dispersion analysis, that accounts for the dispersion created by diffusioosmotic flow from the channel sidewalls. We derive the effective dispersion coefficient and validate our results by comparing them with direct numerical simulations. We also compare our model with experiments and obtain quantitative agreement for a wide range of colloidal particle sizes. Our analysis reveals two important conclusions. First, in the absence of mean flow, dispersion is driven by the flow created by diffusioosmotic wall slip such that spreading can be reduced by decreasing the channel wall diffusioosmotic mobility. Second, the model can explain the spreading of colloids in a dead-end pore for a wide range of particle sizes. We note that while the analysis presented here focuses on a dead-end pore geometry with no mean flow, our theoretical framework is general and can be adapted to other geometries and other background flows.

Key words: Authors should not enter keywords on the manuscript, as these must be chosen by the author during the online submission process and will then be added during the typesetting process (see http://journals.cambridge.org/data/relatedlink/jfm-keywords.pdf for the full list)

---

† Email address for correspondence: hastone@princeton.edu

1. Introduction

Diffusiophoresis has been studied as a mechanism for the motion of colloidal particles due to chemical gradients since its discovery by Derjaguin *et al.* (1947). In recent microfluidic studies (Shin *et al.* 2016; Ault *et al.* 2017; Battat *et al.* 2019; Gupta *et al.* 2020*b*; Wilson *et al.* 2020; Singh *et al.* 2020; Alessio *et al.* 2021), a dead-end pore configuration is used to set up a transient one-dimensional (1D) diffusion of solutes; significant colloidal dispersion is observed, which the typical models are unable to capture. In addition to the dead-end pore geometry, experimental data in other microfluidic configurations has been reported in which colloidal dispersion can be observed but remains unexplained quantitatively (Ahmed & Stocker 2008; Abécassis *et al.* 2008, 2009; Palacci *et al.* 2010, 2012; McDermott *et al.* 2012; Paustian *et al.* 2015; Nery-Azevedo *et al.* 2017; Shimokusu *et al.* 2019).

The reports in the literature do acknowledge that diffusioosmosis along the channel walls induces flow of the bulk liquid, which causes colloidal dispersion (Keh & Ma 2005; Kar *et al.* 2015; Shin *et al.* 2016, 2017; Ault *et al.* 2019; Rasmussen *et al.* 2020). However, only a few studies have combined the influences of diffusiophoresis and diffusioosmosis in order to investigate particle motion in more realistic settings (Shin *et al.* 2017; Singh *et al.* 2020; Williams *et al.* 2020; Alessio *et al.* 2021). In our previous article, for a configuration showing compaction of particles, we demonstrated that particle motion due to diffusiophoresis and a diffusioosmotic-slip driven flow field that neglects the smallest dimension of the pore does predict a non-zero dispersion of colloids (Alessio *et al.* 2021). Physically, diffusioosmosis along the sidewalls creates a flow structure that stretches the particle distribution along the pore, and generates an apparent motion of particles that is analogous to Taylor dispersion (Taylor 1953; Aris 1956; Doshi *et al.* 1978; Stone & Brenner 1999; Aminian *et al.* 2016; Chu *et al.* 2021; Migacz & Ault 2022). Still, our two-dimensional (2D) model yielded a lower quantitative dispersion value than experiments and thus the agreement between the model and experiments remained qualitative.

To enable widespread use of diffusiophoresis in lab-on-a-chip applications such as energy storage and desalination devices (Gupta *et al.* 2020*a*,*c*; Bone *et al.* 2020), particle separation (Lee *et al.* 2018; Seo *et al.* 2020; Shin 2020), colloidal focusing and delivery (Banerjee *et al.* 2016; Shi *et al.* 2016; Gandhi *et al.* 2020), ion-exchange membranes (Florea *et al.* 2014), zeta potential measurement (Shin *et al.* 2017), and macromolecule transport in biological systems (Bruno *et al.* 2018; Hartman *et al.* 2018; Yang *et al.* 2018), understanding and quantifying dispersion is crucial. Recently, studies have modeled the dispersion of a patch of particles that spread due to diffusiophoresis (Raynal & Volk 2019; Gupta *et al.* 2020*b*; Chu *et al.* 2020, 2021; Migacz & Ault 2022). However, these studies assume a model configuration where the flow due to sidewalls is not considered. In practice, since the concentration gradients are often created in a microfluidic configuration, there is diffusioosmotic flow present due to the sidewalls. To this end, the objective of this article is to quantify the effect of dispersion that arises from the diffusioosmotic flow.

To achieve the aforementioned objective, in our modeling approach, we now consider the three-dimensional flow that arises from the sidewalls, and present a Taylor dispersion analysis for fast and convenient calculation of dispersion. Additionally, in our experiments, we modified the dead-end pore configuration to observe the dispersion of a patch of particles, which enables an easier and more direct comparison with the model. In particular, in §2 we present dead-end pore experiments demonstrating typical scenarios that require understanding of the 3D flow structure. By using a particle patch in pores with the same width but different heights, we show that simpler 1D and 2D models

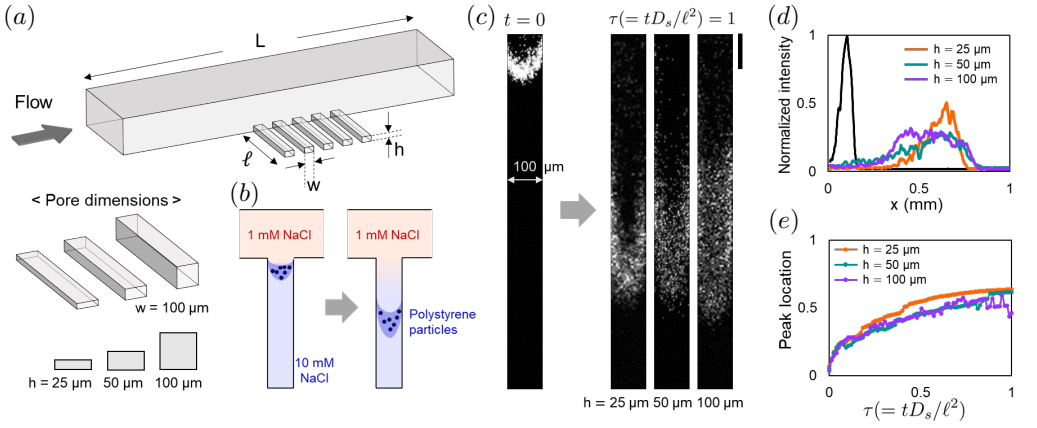

FIGURE 1. Diffusiophoresis and diffusioosmosis-induced dispersion of a patch of particles in a dead-end pore. (*a*) Schematic of a microfluidic channel with dead-end pores of length ℓ. Pores with different heights ($h = 25,\ 50$, and 100 μm) were tested in our experiments. (*b*) Schematic of an experiment using a particle patch that invades the pore. Details of the experimental setup are explained in §5. (*c*) Fluorescent images obtained from dead-end pore experiments. Particle distributions in pores of three different heights are shown. Scale bar is 100 μm. (*d*) Pore-width-averaged intensity plotted versus distance along the pore (x). The profiles are obtained at non-dimensional time $\tau = tD_s/\ell^2 = 1$, where D_s is the solute diffusivity. (*e*) Peak locations measured in the experiments are plotted versus non-dimensional time.

cannot provide sufficient information about the particle distribution since they lack the details of the velocity that drive the dispersion. In §3, we derive the generic form of the 1D cross-sectional average of the advective-diffusion equation for particles undergoing diffusiophoresis in the flow field set up by diffusioosmosis along the walls, with specific forms of the 1D representation of model 2D pore and 3D pores presented in Appendix A. In §4, analyses of the dispersion equations are presented for various system parameters including the pore geometry and the properties of particles and walls. Finally, in §5, a detailed comparison is made of the experiments and the 1D model representation of the 3D pores, where the particle size is varied to investigate the effect of changing the particle rate of diffusion on the overall dispersion. We find good agreement with the predictions of the cross-sectional average model for long-pore systems.

2. Diffusiophoresis of a patch of particles in a dead-end pore geometry

We use dead-end pore geometries with different heights to demonstrate diffusiophoresis of a particle patch and the influence of diffusioosmosis. A finite number of particles are introduced at the inlet of dead-end pores of the same width and length ($w = 100$ μm and $\ell = 1$ mm), and different heights ($h = 25,\ 50$, and 100 μm; figure 1(a, b)). Initially, a concentration gradient of NaCl is established by filling the pore with a 10 mM solution and the main channel, in which there is flow, with a 1 mM solution; the injected particles are then advected into the pore by diffusiophoresis. Experimental details for establishing the initial condition are explained in §5.

Transport of the particle patch in the three pores looks similar at the beginning, but we observe quantitative differences as the particle distribution evolves in pores with different cross-sectional aspect ratios (figure 1(c)). Because the effect of different h is not captured in the two-dimensional (2D) analyses that neglect the effect of the smallest dimension of

the pore, i.e., considering a model pore with ℓ and w as its dimensions, the experimental results in figure 1(c) suggest that differences in the particle distribution cannot be simply explained by such 2D models.

Since the particle distribution varies in the experiments in the three different pores, the peak location can be obtained by analyzing the pore-width-averaged intensity profiles (figure 1(d)). We observe that the peak locations measured in the three pores are similar up to dimensionless time $\tau = tD_\mathrm{s}/\ell^2 \approx 0.1$, where D_s is the diffusivity of Na^+ ions, but deviate from each other at later times (figure 1(e)). The width-averaged intensity plotted versus distance along the pore motivates the question of determining an effective 1D representation of the particle transport.

As we demonstrate below, diffusiophoresis and diffusioosmosis acting in tandem result in the transport and spreading of the particle patch that is analogous to the flow-driven dispersion that occurs in pressure-driven flow in a rectangular channel. For example, for the flow-driven dispersion in a pipe flow (Taylor 1953; Aminian *et al.* 2016), particles move on average with the mean flow speed and dispersion about the mean occurs due to Brownian motion as well as the non-uniform velocity profile throughout the cross section of the channel. In our experiments, particles translate into the pore with the (transient) diffusiophoretic speed, and the wall-driven diffusioosmotic flow velocity stretches the particle distribution along the pore. Note that mass conservation inside the dead-end pore enforces zero net volumetric flux for the fluid, and the velocity distribution in the channel cross section drives the axial dispersion of the particle patch. Therefore, for a particle patch that moves along the narrow pore with the diffusiophoretic velocity, we next apply Taylor dispersion analysis, within the lubrication approximation, to account for the flow structure in the rectangular cross section to obtain a simplified 1D description of the particle distribution.

3. Derivation of a 1D cross-sectionally averaged concentration equation for colloids undergoing diffusiophoresis in a diffusioosmotic slip-driven flow

For the channel flow configurations of interest here, the concentration N of colloidal particles undergoing diffusiophoresis can be described by an advective-diffusion equation. The particles diffuse at characteristic rate D_p relative to the mean fluid velocity and advect due to both a diffusiophoretic velocity field $\boldsymbol{v}_\mathrm{DP}$ and a fluid flow field $\boldsymbol{v}_\mathrm{f}$ produced by a diffusioosmotic slip velocity $\boldsymbol{v}_\mathrm{s}$ on the channel walls. Both the diffusiophoretic $\boldsymbol{v}_\mathrm{DP}$ and diffusioosmotic slip $\boldsymbol{v}_\mathrm{s}$ velocities are driven by the diffusion of a background solute with concentration C such that $\boldsymbol{v}_\mathrm{DP} \propto \boldsymbol{\nabla} \log C$ and $\boldsymbol{v}_\mathrm{s} \propto \boldsymbol{\nabla} \log C$. We introduce the particle velocity $\boldsymbol{v}_\mathrm{p} = \boldsymbol{v}_\mathrm{f} + \boldsymbol{v}_\mathrm{DP}$ and write the advective-diffusion equation

$$\frac{\partial N}{\partial t} + \boldsymbol{\nabla} \cdot (\boldsymbol{v}_\mathrm{p} N) = D_\mathrm{p} \nabla^2 N. \tag{3.1}$$

Previous studies compare dead-end pore experiments to numerical solutions of the 1D advective-diffusion equation (Gupta *et al.* 2020*b*; Wilson *et al.* 2020; Ault *et al.* 2017; Chu *et al.* 2020), which exclude $\boldsymbol{v}_\mathrm{f}$. While this approach simplifies calculations and provides for a qualitative comparison of the mean colloidal motion, it leaves out the effect of spreading of the particles due to the flow field. By introducing a Taylor dispersion model, we account for flow-driven spreading effects in a 1D equation for the cross-sectionally averaged colloid distribution. In this section, we derive a general form of this 1D effective transport equation.

We consider a pore with axial dimension $x = \boldsymbol{x} \cdot \boldsymbol{e}_x$. The typical scale of the fluid

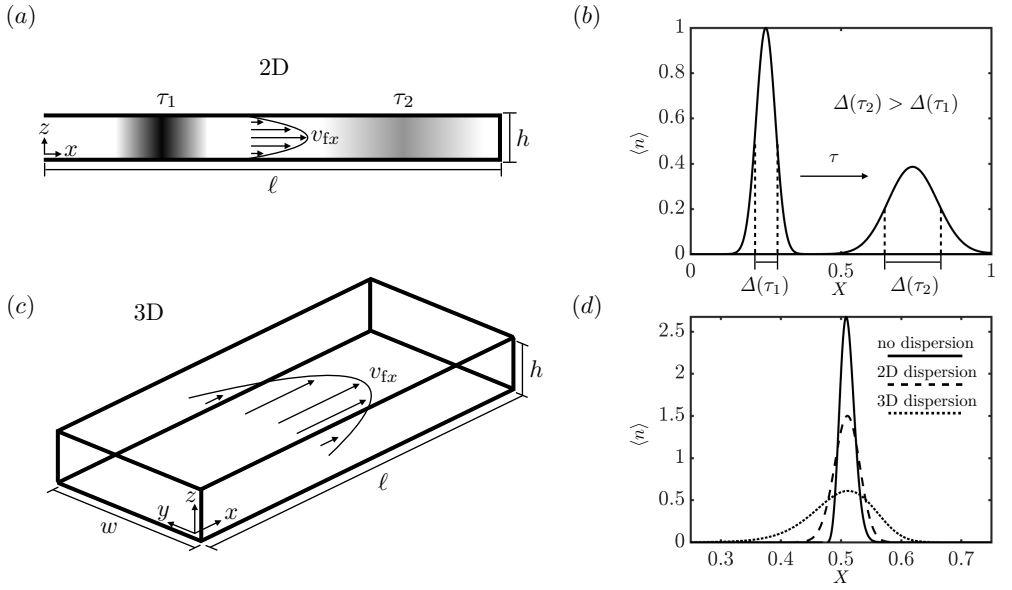

FIGURE 2. Schematic of 2D and 3D descriptions of the velocity profile in dead-end pores, depicted in panels (*a*) and (*c*), respectively. Coordinate axes are defined with the origin at the upstream corner. Pore length, height, and width are defined, respectively, as ℓ, h, and w. Velocity profiles are depicted in the $x-$direction. Dispersion of the colloid concentration over timescale $\tau = \tau_1 \to \tau_2$ is depicted in the 2D description (panel (*a*)) and the cross-sectional average of the colloid concentration is shown in panel (*b*), where the full width half maximum Δ is visually defined as the distance between the two points in the distribution with values of half the maximum. Panel (*d*) is a qualitative plot demonstrating the effect of dispersion on a colloid distribution. Introducing a third dimension, as depicted in panel (*c*), causes an increase in dispersion, as is well known in the Taylor dispersion literature (Chatwin & Sullivan 1982).

velocity ($\boldsymbol{v}_\mathrm{f}$) is on the order of magnitude of the wall slip velocity ($v_\mathrm{s} \approx \Gamma_\mathrm{w}/\ell$, where Γ_w and ℓ are, respectively, the diffusioosmotic mobility and pore length), and an estimate of the Péclet number for the solute, $Pe_\mathrm{s} = v_\mathrm{s}\ell/D_\mathrm{s}$ where D_s is the solute diffusivity, yields $Pe_\mathrm{s} \approx \Gamma_\mathrm{w}/D_\mathrm{s} \lesssim 1$ (Gupta *et al.* 2020*b*). Therefore, inside a narrow dead-end pore, the solute concentration field $C(x,t)$ can be assumed one-dimensional so that 1D diffusiophoresis of particles is achieved, i.e., $\boldsymbol{v}_\mathrm{DP} = v_\mathrm{DP}\boldsymbol{e}_x$.

Defining the perpendicular components of the position vector as $\boldsymbol{x}_\perp \equiv \boldsymbol{x} - x\boldsymbol{e}_x$, away from the pore entrance the velocity fields have the form of a wall slip velocity $\boldsymbol{v}_\mathrm{s} = v_\mathrm{s}(x,t)\boldsymbol{e}_x$, fluid velocity $\boldsymbol{v}_\mathrm{f}(\boldsymbol{x},t) = v_\mathrm{s}(x,t)f_x(\boldsymbol{x}_\perp,t)\boldsymbol{e}_x + \boldsymbol{v}_{\mathrm{f}\perp}(\boldsymbol{x},t)$, where $\boldsymbol{e}_x \cdot \boldsymbol{v}_{\mathrm{f}\perp} = 0$, and $\boldsymbol{v}_\mathrm{DP} = v_\mathrm{DP}(x,t)\boldsymbol{e}_x$, where we assume an incompressible flow such that $\boldsymbol{\nabla} \cdot \boldsymbol{v}_\mathrm{f} = 0$. The advective-diffusion equation (3.1) becomes

$$\frac{\partial N}{\partial t} + \boldsymbol{v}_\mathrm{f} \cdot \boldsymbol{\nabla} N + \frac{\partial}{\partial x}(v_\mathrm{DP} N) = D_\mathrm{p}\nabla^2 N. \tag{3.2}$$

This equation can be solved numerically for N, although to do so would require a 2D or 3D computational scheme. To simplify our calculations, we revisit the analysis of Taylor (1953) to derive a 1D equation for the cross-sectionally averaged concentration by integrating the effects of the fluid flow, with the important differences that the fluid velocity field in the pore here has zero cross-sectional average and varies in x and t according to v_s; note that $\boldsymbol{v}_\mathrm{f}$ varies with the transverse coordinates and time.

We start by defining the perturbation concentration $N'(\boldsymbol{x},t)$:

$$N'(\boldsymbol{x},t) = N(\boldsymbol{x},t) - \langle N\rangle(x,t), \tag{3.3}$$

where the cross-sectional average is defined as:

$$\langle f\rangle(x,t) = \frac{1}{A}\int_A f \,\mathrm{d}A' \tag{3.4}$$

for cross-sectional area A with normal vector in the $x-$direction. We expand (3.2) using these definitions to find

$$\frac{\partial}{\partial t}(\langle N\rangle + N') + v_{\mathrm{f}x}\frac{\partial\langle N\rangle}{\partial x} + \boldsymbol{v}_{\mathrm{f}}\cdot\boldsymbol{\nabla}N' + \frac{\partial}{\partial x}(v_{\mathrm{DP}}(\langle N\rangle + N')) = D_{\mathrm{p}}\left(\frac{\partial^2\langle N\rangle}{\partial x^2} + \nabla^2 N'\right) \tag{3.5}$$

and take the cross-sectional average, which yields

$$\frac{\partial\langle N\rangle}{\partial t} + \langle \boldsymbol{v}_{\mathrm{f}}\cdot\boldsymbol{\nabla}N'\rangle + \frac{\partial}{\partial x}(v_{\mathrm{DP}}\langle N\rangle) = D_{\mathrm{p}}\frac{\partial^2\langle N\rangle}{\partial x^2}, \tag{3.6}$$

where we have used, by definition, $\langle N'\rangle = 0$, $\langle v_{\mathrm{f}x}\rangle = 0$, and $\partial\langle N\rangle/\partial\boldsymbol{x}_\perp = \boldsymbol{0}$.

Now we subtract (3.6) from (3.2) to obtain (still an exact expression)

$$\frac{\partial N'}{\partial t} + v_{\mathrm{f}x}\frac{\partial\langle N\rangle}{\partial x} + \boldsymbol{v}_{\mathrm{f}}\cdot\boldsymbol{\nabla}N' - \langle \boldsymbol{v}_{\mathrm{f}}\cdot\boldsymbol{\nabla}N'\rangle + \frac{\partial}{\partial x}(v_{\mathrm{DP}}N') = D_{\mathrm{p}}\nabla^2 N', \tag{3.7}$$

at which point we must make approximations to go further. As originally developed by Taylor (1953), we consider the lubrication approximation:

$$\left|\nabla_\perp^2 N'\right| \gg \left|\frac{\partial^2 N'}{\partial x^2}\right|, \tag{3.8}$$

where we define $\nabla_\perp^2 \equiv \nabla^2 - \partial^2/\partial x^2$. Assuming $O(v_{\mathrm{DP}}) = O(v_{\mathrm{f}x})$, $|N'| \ll N$, we apply the approximation

$$O\left(v_{\mathrm{f}x}\frac{\partial\langle N\rangle}{\partial x}\right) \gg O\left(\boldsymbol{v}_{\mathrm{f}}\cdot\boldsymbol{\nabla}N',\ \langle \boldsymbol{v}_{\mathrm{f}}\cdot\boldsymbol{\nabla}N'\rangle,\ \frac{\partial}{\partial x}(v_{\mathrm{DP}}N')\right). \tag{3.9}$$

Finally, assuming the perturbation concentration becomes independent of the initial particle distribution, we take the steady-state limit $\partial N'/\partial t \to 0$ to arrive at an equation for the perturbation concentration,

$$v_{\mathrm{f}x}\frac{\partial\langle N\rangle}{\partial x} = D_{\mathrm{p}}\nabla_\perp^2 N', \tag{3.10}$$

which must be solved for $N'(\boldsymbol{x})$ by applying no-flux conditions at the pore walls and requiring that $\langle N'\rangle = 0$. Equation (3.10) is analogous to the equation for the perturbation field of a solute obtained in the original analysis of Taylor (1953). The steady-state limit neglects the effect on $\partial N'/\partial t$ of the time-dependence of v_{f}, which arises from the time-dependence of v_{s}. This is equivalent to assuming that the colloids reach a steady-state distribution throughout the cross section instantaneously upon a change in v_{f}. We justify this assumption by comparing the time-scale of particle diffusion through the cross section, A/D_{p}, where A is the cross-sectional area, to the time-scale of axial particle transport, ℓ/v_{DP}. Introducing particle diffusiophoretic mobility Γ_{p}, we have $v_{\mathrm{DP}} \approx \Gamma_{\mathrm{p}}/\ell$. Furthermore, as the diffusiophoretic motion cannot outpace its source, the diffusion of the solute, we can write $v_{\mathrm{DP}} \lesssim D_{\mathrm{s}}/\ell$. Thus, for any system that obeys $A/\ell^2 \ll D_{\mathrm{p}}/D_{\mathrm{s}}$, the steady-state limit $\partial N'/\partial t \to 0$ is valid.

Motivated by (3.10), it is convenient to define the quantities:

$$f_x(\boldsymbol{x}_\perp) = \frac{v_{\mathrm{f}x}(\boldsymbol{x},t)}{v_{\mathrm{s}}(x,t)}, \tag{3.11a}$$

$$N' = v_{\mathrm{s}}(x,t)\frac{\partial \langle N\rangle}{\partial x}\frac{f_{N'}(\boldsymbol{x}_\perp)}{D_{\mathrm{p}}}, \tag{3.11b}$$

$$\nabla_\perp^2 f_{N'} = -f_x(\boldsymbol{x}_\perp), \tag{3.11c}$$

where (3.11c) is to be solved with no-flux boundary conditions at the pore walls and the requirement that $\langle f_{N'}\rangle = 0$.

The quantity $\langle \boldsymbol{v}_{\mathrm{f}} \cdot \boldsymbol{\nabla} N'\rangle$ therefore has the form

$$\langle \boldsymbol{v}_{\mathrm{f}} \cdot \boldsymbol{\nabla} N'\rangle = \left\langle v_{\mathrm{s}} f_x \frac{\partial N'}{\partial x} + \boldsymbol{v}_{\mathrm{f}\perp} \cdot \boldsymbol{\nabla}_\perp N' \right\rangle = \left\langle v_{\mathrm{s}} f_x \frac{\partial N'}{\partial x} + \boldsymbol{\nabla}_\perp \cdot (\boldsymbol{v}_{\mathrm{f}\perp} N') - N' \boldsymbol{\nabla}_\perp \cdot \boldsymbol{v}_{\mathrm{f}\perp} \right\rangle. \tag{3.12}$$

Applying the incompressible flow condition,

$$\boldsymbol{\nabla} \cdot \boldsymbol{v}_{\mathrm{f}} = f_x \frac{\partial v_{\mathrm{s}}}{\partial x} + \boldsymbol{\nabla}_\perp \cdot \boldsymbol{v}_{\mathrm{f}\perp} = 0, \tag{3.13}$$

we substitute for $\boldsymbol{\nabla}_\perp \cdot \boldsymbol{v}_{\mathrm{f}\perp}$ and apply the product rule of differentiation to obtain

$$\langle \boldsymbol{v}_{\mathrm{f}} \cdot \boldsymbol{\nabla} N'\rangle = \left\langle f_x \frac{\partial}{\partial x}(v_{\mathrm{s}} N') + \boldsymbol{\nabla}_\perp \cdot (\boldsymbol{v}_{\mathrm{f}\perp} N') \right\rangle. \tag{3.14}$$

With the definitions of the cross-sectional area average in (3.4) and the perpendicular derivative vector $\boldsymbol{\nabla}_\perp$, denoting $\boldsymbol{e}_\perp$ as the normal vector to the boundary, using the divergence theorem, and noting that there is zero fluid penetration at the pore walls, we finally arrive at

$$\langle \boldsymbol{\nabla}_\perp \cdot (\boldsymbol{v}_{\mathrm{f}\perp} N')\rangle = \frac{1}{A}\oint \boldsymbol{e}_\perp \cdot \boldsymbol{v}_{\mathrm{f}\perp} N' \, \mathrm{d}s = 0, \tag{3.15}$$

where the line integral is performed over the boundaries of the pore cross section. This simplifies (3.14) by eliminating the perpendicular velocity components. Invoking the definition in (3.11c), we have the result

$$\langle \boldsymbol{v}_{\mathrm{f}} \cdot \boldsymbol{\nabla} N'\rangle = -\frac{1}{D_{\mathrm{p}}} \langle f_x f_{N'}\rangle \frac{\partial}{\partial x}\left(v_{\mathrm{s}}^2 \frac{\partial \langle N\rangle}{\partial x}\right). \tag{3.16}$$

Substituting this result into (3.6), we have a one-dimensional PDE for the cross-sectionally averaged colloid concentration,

$$\frac{\partial \langle N\rangle}{\partial t} = \frac{\partial}{\partial x}\left(K \frac{\partial \langle N\rangle}{\partial x} - v_{\mathrm{DP}} \langle N\rangle \right), \tag{3.17}$$

where the modified diffusion coefficient is defined as:

$$K \equiv D_{\mathrm{p}} + \frac{1}{D_{\mathrm{p}}} \langle f_x f_{N'}\rangle \left(v_{\mathrm{s}}(x,t)\right)^2. \tag{3.18}$$

In Appendix A we calculate $\langle f_x f_{N'}\rangle$ by solving (3.11c) for the forms of $v_{\mathrm{f}x}$ in both the 2D and 3D narrow pores depicted in figure 2. We note that the results are equivalent to the well-known 2D result and additionally the 3D result introduced by Chatwin & Sullivan (1982) upon replacing the diffusioosmotic slip velocity with the mean velocity of a pressure-driven flow. Furthermore, the elements of our Taylor dispersion model have

been introduced in part by previous studies. For example, Chu *et al.* (2021) present a Taylor dispersion model of diffusiophoretic motion of particles; however the flow field is driven by an external pressure gradient and does not include the effect of a diffusioosmotic slip-driven flow field. Furthermore, due to their use of cylindrical geometry, they do not examine the effect of the channel cross section aspect ratio on the dispersion. It would be straightforward to include features of their model such as a colloidal reaction term, an externally-driven flow, and a cylindrical channel geometry into our model. Migacz & Ault (2022) also present a Taylor dispersion model of diffusiophoretic colloids with an externally-driven flow field; their focus is on a narrow two-dimensional channel for which they neglect the diffusioosmotic wall slip. It would be straightforward to include in our model the zeta potential dependence on the solute concentration featured in their model, although to incorporate their characterization of early-time dynamics requires further research. Stone & Brenner (1999) present a dispersion model for radial outflow between two disks, which exhibits streamwise variation in the mean velocity. Our model of diffusiophoresis and diffusioosmosis generalizes the above studies by including a multi-directional, longitudinal direction-dependent and time-dependent flow with zero mean in a channel geometry, allowing for accurate direct comparison of the model to dead-end pore diffusiophoresis experiments (see section 5).

4. Analysis of dispersion equations

4.1. *Comparison of the dispersion equation to the two-dimensional advective-diffusion equation*

Numerical solutions for the diffusiophoretic motion of colloids in a 2D dead-end pore (figure 2(a)) based on (3.1) are compared to numerical simulations of the dispersion model based on (3.17-3.18). The 2D pore is simulated in order to validate our Taylor dispersion model with numerical tests; for comparison to our experiments, a 3D model must be implemented. We introduce non-dimensional quantities $\boldsymbol{X} = \boldsymbol{x}/\ell$, $\boldsymbol{V} \equiv \boldsymbol{v}\ell/D_\mathrm{s}$ (for all velocities), $\tau \equiv tD_\mathrm{s}/\ell^2$, and $n \equiv N/N_0$, where N_0 is the initial maximum concentration of the colloid, ℓ is the pore length as depicted in figure 2, and D_s is the characteristic diffusivity of the diffusing solute whose gradient drives the colloid diffusiophoresis and the diffusioosmotic slip velocity on the pore walls. For simplicity we consider a monovalent, binary salt as the solute, whose concentration can be described by one quantity. We define C as the concentration of the solute, which is made non-dimensional by $c \equiv C/C_0$ for initial maximum concentration C_0. Substituting in our non-dimensional quantities, (3.1) becomes

$$\frac{\partial n}{\partial \tau} + \boldsymbol{\nabla} \cdot (\boldsymbol{V}_\mathrm{p} n) = \frac{D_\mathrm{p}}{D_\mathrm{s}} \nabla^2 n, \tag{4.1}$$

where we redefine $\boldsymbol{\nabla} \equiv [\partial/\partial X, \partial/\partial Y]$ and note that the velocity $\boldsymbol{V}_\mathrm{p} = \boldsymbol{V}_\mathrm{f} + \boldsymbol{V}_\mathrm{DP}$ is the sum of the fluid and diffusiophoretic velocities. We define the non-dimensional modified diffusion coefficient as

$$\mathcal{K} \equiv \frac{D_\mathrm{p}}{D_\mathrm{s}} + \frac{V_\mathrm{s}^2}{D_\mathrm{p}/D_\mathrm{s}} \frac{\langle f_X f_{n'} \rangle}{\ell^2}, \tag{4.2}$$

where $\langle f_X f_{n'} \rangle / \ell^2 \equiv \langle f_x f_{N'} \rangle = (h/\ell)^2/210$, well-known for pressure-driven parabolic flow in a 2D channel, is computed in Appendix A, see (A 6). We see that introducing the non-dimensional quantities reveals a set of two non-dimensional parameters to describe our

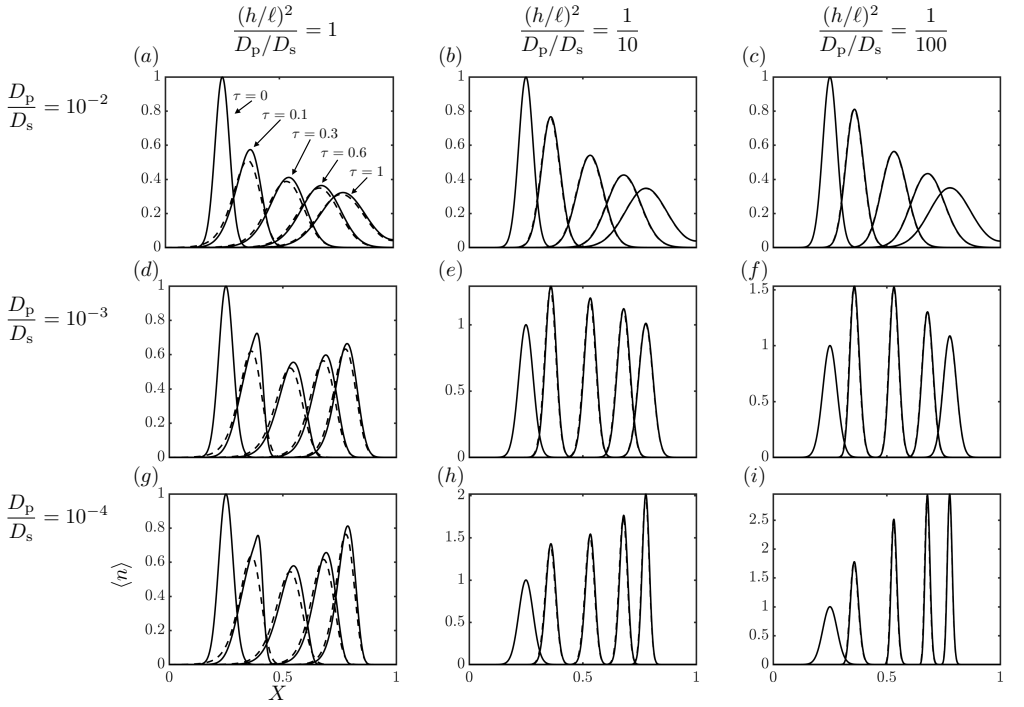

FIGURE 3. Comparison of the cross-sectionally averaged diffusiophoretic colloid concentration $\langle n \rangle$ in a dead-end pore with diffusioosmotic slip-driven flow at the walls. Solid lines show numerical solutions to the full 2D model, (4.1), and dashed lines show numerical solutions to the one-dimensional model with 2D dispersion, (4.3) and (A 6). The two different numerical solutions have matching initial Gaussian distributions and no-flux conditions at the pore walls and inlet. The diffusiophoretic velocity and the diffusioosmotic slip are driven by a solute diffusing out of the pore into an infinite reservoir. The initial solute condition is $\langle c \rangle (\tau = 0) = 1$ and the boundary conditions are $\langle c \rangle (X = 0) = 0.1$ and no-flux conditions at the pore walls. Three diffusivities of the colloidal particles and three pore heights are considered. Excellent agreement is observed between the two models for $(h/\ell)^2 = D_\mathrm{p}/D_\mathrm{s}/10$ and $(h/\ell)^2 = D_\mathrm{p}/D_\mathrm{s}/100$, as predicted by the Taylor dispersion limit (4.9), and consistent with the steady-state limit $\partial N'/\partial t \to 0$.

system: $D_\mathrm{p}/D_\mathrm{s}$ and h/ℓ. Now making (3.17) non-dimensional, we have

$$\frac{\partial \langle n \rangle}{\partial \tau} = \frac{\partial}{\partial X}\left(\mathcal{K}\frac{\partial \langle n \rangle}{\partial X} - V_\mathrm{DP}\langle n \rangle\right). \tag{4.3}$$

Equation (4.2) can be adapted to describe the solute concentration c:

$$\frac{\partial \langle c \rangle}{\partial \tau} = \frac{\partial}{\partial X}\left(\mathcal{K}_\mathrm{s}\frac{\partial \langle c \rangle}{\partial X} - V_\mathrm{f}\langle c \rangle\right), \tag{4.4}$$

where we define the solute modified diffusion coefficient as

$$\mathcal{K}_\mathrm{s} \equiv 1 + \frac{(h/\ell)^2}{210}V_\mathrm{s}^2. \tag{4.5}$$

As described in §3, with a solute Péclet number $Pe_\mathrm{s} \approx \Gamma_\mathrm{w}/D_\mathrm{s} \lesssim 1$ the solute concentration is approximately one-dimensional and can be accurately calculated with a 1D diffusion equation. This ensures furthermore that the solute concentration can be calculated with the dispersion equations (4.4 and 4.5) in the lubrication approximation (Taylor 1953; Aris 1956; Chu *et al.* 2021), with accuracy greater than or equal to the simple diffusion model. We include the dispersion effect on the solute as a general description of

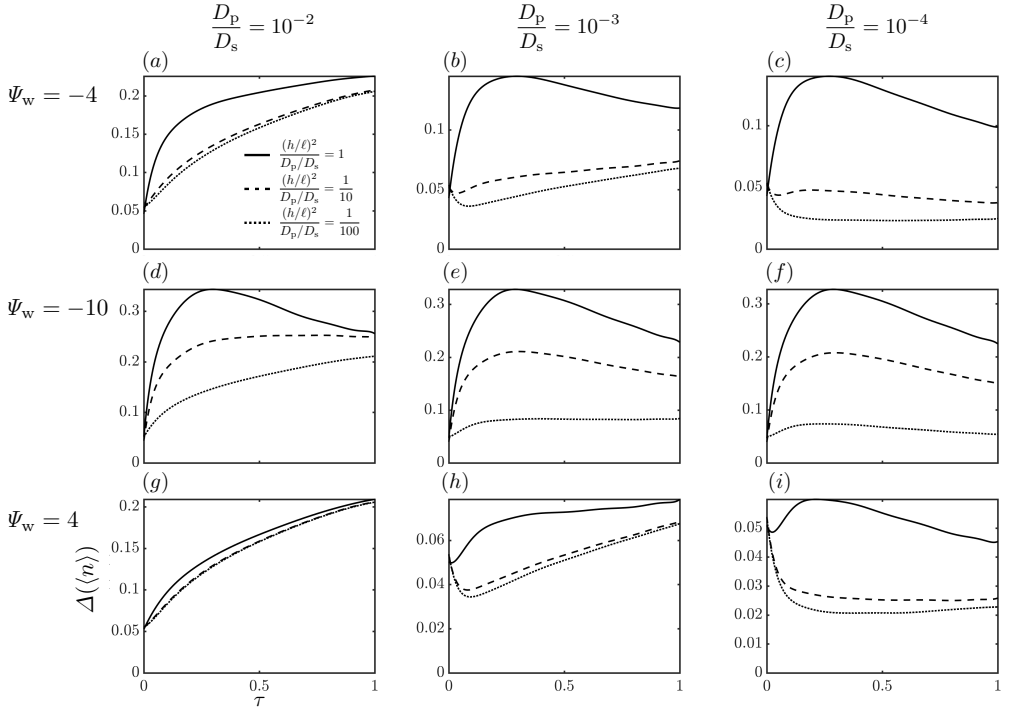

FIGURE 4. The full width half maximum $\Delta(\langle n \rangle)$ (see figure 2b) versus time τ of colloidal particle distributions $\langle n \rangle$, as obtained by solving (4.3) and (A 6). The colloid distributions have Gaussian initial distributions and no-flux conditions at the pore walls and inlet. The diffusiophoretic velocity and the diffusioosmotic wall slip are driven by a solute diffusing out of the pore into an infinite reservoir. The initial solute concentration is $\langle c \rangle (\tau = 0) = 1$ and the boundary conditions are $\langle c \rangle (X = 0) = 0.1$ and no-flux conditions at the pore walls. The full width half maximum is compared for varying particle diffusivity ($D_p/D_s = 10^{-2},\ 10^{-3},\ 10^{-4}$) and varying pore wall zeta potential ($\Psi_w = -4,\ -10,\ 4$). Furthermore, each panel shows the full width half maximum for three values of the ratio $(h/\ell)^2/(D_p/D_s)$: 1, 1/10, and 1/100.

our model. Comparisons between the dispersion model and a one-dimensional diffusion model of the low Péclet number solute revealed only minor differences.

We assume constant particle and wall zeta potentials and a vanishing ratio of Debye length to particle radius. Therefore, the diffusiophoretic and diffusioosmotic velocities v_{DP} and v_s depend on the constant particle and wall zeta potentials $\psi_{p,w}$, the gradient of the logarithm of the solute concentration, and the diffusivity difference factor $\beta = (D_+ - D_-)/(z_+ D_+ - z_- D_-)$ of the electrolyte with ionic diffusivities D_+ and D_- and valences z_+ and z_-. The zeta potentials are made non-dimensional by defining $\Psi = e\psi/(k_B T)$, where e is the elementary charge, k_B is the Boltzmann constant, and T is the absolute temperature of the solution. It is convenient to introduce the velocity prefactor $\alpha = \epsilon k_B^2 T^2/(e^2 \mu D_s)$, where ϵ is the electrical permittivity of the solution and μ is the solution viscosity. We define diffusiophoretic mobility Γ_p and diffusioosmotic mobility Γ_w, which are made non-dimensional by the solute diffusivity and related to the particle and wall zeta potentials by the approximate form (Prieve *et al.* 1984; Velegol *et al.* 2016; Keh & Ma 2005):

$$\frac{\Gamma_{p,w}}{D_s} = \alpha \left(\beta \Psi_{p,w} + \frac{\Psi_{p,w}^2}{8} \right). \tag{4.6}$$

The diffusiophoretic velocity and the diffusioosmotic slip velocity are then given by:

$$\boldsymbol{V}_{\mathrm{DP}} = \frac{\Gamma_{\mathrm{p}}}{D_{\mathrm{s}}} \boldsymbol{\nabla} \log c, \tag{4.7a}$$

$$\text{and } V_{\mathrm{s}} = \frac{\Gamma_{\mathrm{w}}}{D_{\mathrm{s}}} \left[\frac{\partial \log c}{\partial X} \right]_{Z=0,h/\ell}. \tag{4.7b}$$

where $Z = 0$ and $Z = h/\ell$ correspond to the pore walls.

We can consider the Taylor dispersion limits to simplify our expressions for the velocities. Taylor dispersion most accurately models systems with a low Péclet number, which is the ratio of particle transport timescales:

$$Pe_{\mathrm{TD}} \equiv \frac{\text{time scale to diffuse through channel cross section}}{\text{time scale to transport to end of channel}} \ll 1. \tag{4.8}$$

In our system, the mechanism of bulk particle transport along the pore length is the diffusiophoretic velocity. If we reintroduce dimensional quantities, we see that v_{DP} scales with Γ_{p}/ℓ. The diffusiophoretic mobility Γ_{p} cannot be greater than D_{s}, the characteristic diffusivity of the solute. This gives us the condition

$$\left(\frac{h}{\ell}\right)^2 \ll \frac{D_{\mathrm{p}}}{D_{\mathrm{s}}} \tag{4.9}$$

for which we expect our Taylor dispersion model to describe 2D pore diffusiophoresis and diffusioosmosis with reasonable accuracy. The equivalent condition for the dispersion of the solute would be $(h/\ell)^2 \ll 1$, which is always true in the lubrication approximation that we have employed for the velocity profiles. Therefore, we can approximate all $c(\boldsymbol{X}, \tau)$ with $\langle c \rangle (X, \tau)$, giving us the simplified velocities:

$$V_{\mathrm{DP}} = \frac{\Gamma_{\mathrm{p}}}{D_{\mathrm{s}}} \frac{\partial \log \langle c \rangle}{\partial X}, \tag{4.10a}$$

$$\text{and } V_{\mathrm{s}} = \frac{\Gamma_{\mathrm{w}}}{D_{\mathrm{s}}} \frac{\partial \log \langle c \rangle}{\partial X}. \tag{4.10b}$$

Simulated colloid concentrations from the 2D advective diffusion model (see 4.1) and the 2D reduced-order dispersion model (see 4.3 and A 6) are directly compared in figure 3. Particle diffusivity and the ratio $(h/\ell)^2/(D_{\mathrm{p}}/D_{\mathrm{s}})$ are both varied over three orders of magnitude, demonstrating better agreement of the colloid distributions as the Taylor dispersion limit is better satisfied. Diffusiophoretic focusing is observed in panels $(d)-(i)$, where the colloids increase in concentration as time increases, and is most prominent for the smallest ratios (panels (f) and (i)). This is consistent with the form of (4.2), where an increase in $(h/\ell)^2/(D_{\mathrm{p}}/D_{\mathrm{s}})$ corresponds to an increase in dispersion. Panels $(a)-(c)$ do not demonstrate diffusiophoretic focusing, however, as the large value for particle diffusivity dominates the dispersion effect.

We next report the full width half maximum (defined in figure 2(b)), where larger magnitudes indicate greater dispersion. The full width half maximum as a function of time for the colloid distributions determined from (4.3) and (A 6) are displayed in figure 4. The full width half maximum is compared for varying particle diffusivity across three orders of magnitude and varying pore wall zeta potential: a typical experimental value (Alessio *et al.* 2021) $\Psi_{\mathrm{w}} = -4$ (panels $(a)-(c)$), a strongly negative value $\Psi_{\mathrm{w}} = -10$ (panels $(d)-(f)$), and a positive value $\Psi_{\mathrm{w}} = 4$ (panels $(g)-(i)$). The strongly negative value corresponds to a large slip velocity and thus to increased dispersion. Equation (4.6), considering that β is negative for Na^+ and Cl^-, indicates that the positive

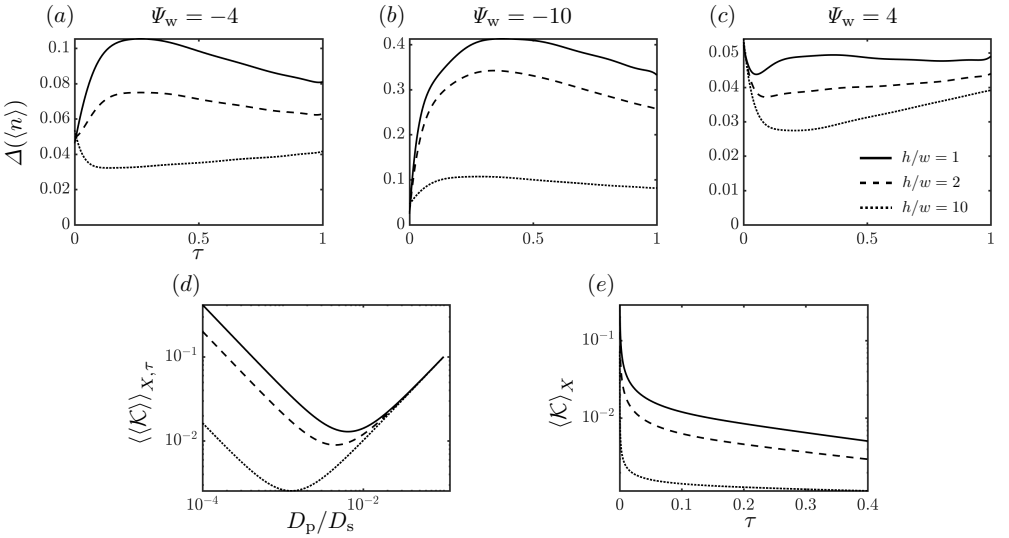

FIGURE 5. $(a)-(c)$ The full width half maximum $\Delta(\langle n \rangle)$ versus time τ of the colloid distributions $\langle n \rangle$ solved from (4.3) and (A 14). The colloid distributions have Gaussian initial distributions and observe no-flux conditions at the pore walls and inlet. The diffusiophoretic velocity and the diffusioosmotic slip are driven by a solute diffusing out of the pore into an infinite reservoir. The initial solute condition is $\langle c \rangle (\tau = 0) = 1$ and the boundary conditions are $\langle c \rangle (X = 0) = 0.1$ and no-flux conditions at the pore walls. The full width half maximum is evaluated for varying pore wall zeta potential ($\Psi_w = -4, -10,\ 4$). (d) The non-dimensional modified coefficient of diffusion $\mathcal{K}$ versus non-dimensional particle diffusivity D_p/D_s. The double bracket indicates an average over the length of the pore and the timespan $\tau = 0 \to 0.4$. A minimum is seen in each curve for an intermediate value of particle diffusivity. (e) The non-dimensional modified coefficient of diffusion versus time. The single bracket indicates an average over the length of the pore. Particle diffusivity is chosen to be $D_p/D_s = 10^{-3}$. A sharp decrease is seen for early times. Each panel demonstrates the effect of increasing cross-sectional aspect ratio h/w to decrease dispersion, indicated by decreasing full width half maximum $(a-c)$ and decreasing modified coefficient of diffusion $(d-e)$.

value corresponds to a small slip velocity and thus to decreased dispersion. Furthermore, each panel shows the full width half maximum of the colloid distribution for three values of the ratio $(h/\ell)^2/(D_p/D_s)$: 1, 1/10, and 1/100. This effect is weakest for the leftmost column (panels (a), (d), and (g)), as the large value of particle diffusivity dominates the dispersion effect similarly to the simulations of figure 3.

4.2. *Parameter analysis of the 3D dispersion equation*

To achieve quantitative agreement between the experiments of §5 and the reduced-order dispersion simulations requires the consideration of the variation of the flow in three spatial dimensions. In Appendix A we introduce the pore width w such that the walls are located at $Y = 0$ and $Y = w/\ell$ and $h < w$, and present the corresponding modified diffusion coefficient.

We modify the model in §4.1 by substituting $\mathcal{K}(X, \tau)$ with the 3D coefficient, defined in (4.2) and (A 14) where $\langle f_X f_{n'} \rangle / \ell^2 \equiv \langle f_x f_{N'} \rangle$, into (4.3). Note that we use the same method to make the coefficient non-dimensional, and furthermore that the non-dimensional coefficient for solute dispersion in (4.4) is replaced with the 3D version in a similar manner. Finally, we include no-flux conditions for each wall of the pore.

The full width half maximum versus time for colloid distributions determined from (4.3) and (A 14) are shown in figure $5(a-c)$. The results indicate enhanced dispersion as

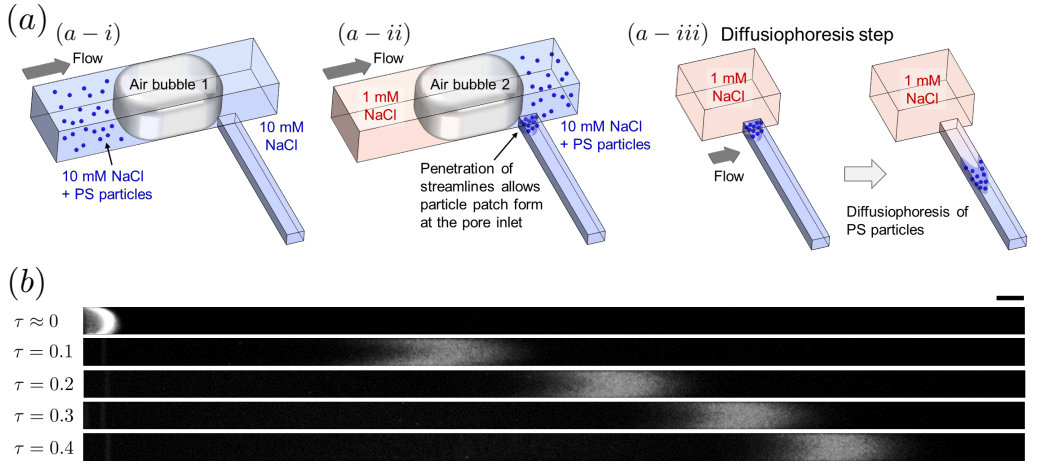

FIGURE 6. Experiments in a long pore ($w = 100$ μm, $h = 50$ μm, and $\ell = 5$ mm). (a) Schematic of typical experimental steps. ($a - i$) The pore is initially filled with the 10 mM NaCl solution. The 10 mM NaCl solution with suspended particles, separated from the original solution by a first air bubble, is flowed in the main channel, then comes in contact with the liquid in the pore. ($a - ii$) Flow in the main channel introduces penetration of streamlines into the pore at the pore inlet (penetration depth $\approx w$), which allows a patch of particles to form at the inlet region of the pore. Then, separated by the second air bubble, a 1 mM NaCl solution is flowed into the main channel to create a concentration gradient in the pore. ($a - iii$) Finally, we obtain diffusiophoresis of a finite number of particles toward the dead-end. (b) Fluorescent images obtained from the experiments with carboxylate-modified polystyrene (c-PS; diameter $d = 0.5$ μm) particles. Image intensity is enhanced for visualization. Original images are included in Appendix C (figure 10). Scale bar is 100 μm.

the width of the distribution increases with stronger dispersion. As in §4.1, we present the effect of pore wall potential Ψ_w on the dispersion in figure 5. Figure 5($d - e$) shows the non-dimensional modified coefficient of diffusion versus the non-dimensional particle diffusivity, averaged across the length of the pore and across the timespan $\tau = 0 \to 0.4$ (panel (d)), and versus time, averaged across the length of the pore (panel (e)). Panel (d) demonstrates a minimum in dispersion for intermediate values of particle diffusivity as predicted by (4.2). Panel (e) highlights how there is a multiple-order-of-magnitude decrease in the modified coefficient of diffusion at early times.

Each panel of figure 5 demonstrates the trend for dispersion to increase as the aspect ratio h/w decreases. This is a natural consequence of dispersion being enhanced by the influence of the side walls. Furthermore, the inclusion of the 3D effect of h/w strictly increases the dispersion of the colloid distributions compared to those calculated from the dispersion model of the 2D channel (Chatwin & Sullivan 1982).

5. Experimental methods and comparison to the one-dimensional equation

We designed experiments using a dead-end pore with $w = 100$ μm, $h = 50$ μm, and $\ell = 5$ mm to compare with the model of the 1D representation of the (three-dimensional) dispersion; $\ell \gg h, w$. Three different particle sizes (diameter $d_p = 1$, 0.5, and 0.2 μm; see Appendix D for particle information) were used to examine the influence of particle diffusivity D_p, which is related to particle diameter by the Boltzmann constant k_B, the absolute temperature T of the solution, and the viscosity μ of the solution through the

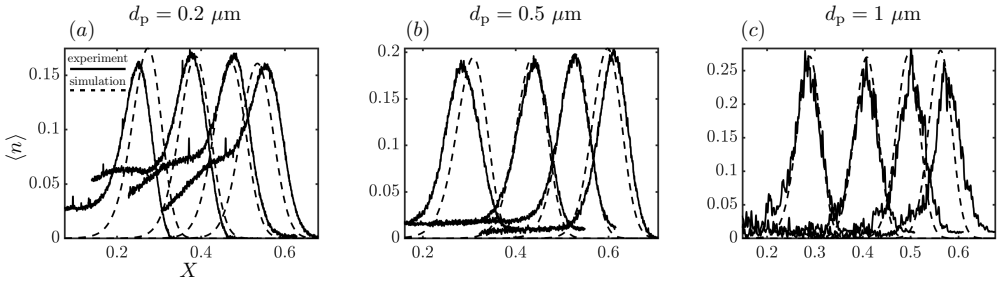

FIGURE 7. Comparison of experimental data (solid) to simulated data (dashed) for different colloidal particle diameters. The concentration distributions in a given experiment, in order of peak location from left to right, correspond to times $\tau = 0.1,\ 0.2,\ 0.3$, and 0.4. Fitting parameters are the dimensionless particle zeta potential Ψ_p and wall zeta potential Ψ_w. Unique values of the fitting parameters were calculated for the simulations of each panel: (*a*) $\Psi_p = -2.84,\ \Psi_w = -3.91$, (*b*) $\Psi_p = -3.31,\ \Psi_w = -3.26$, and (*c*) $\Psi_p = -3.04,\ \Psi_w = -2.06$. Despite a bias due to particle size in the fitted values of the wall zeta potential, there is very good agreement between the experiments and the simulations.

Stokes-Einstein equation:

$$D_p = \frac{k_B T}{3\pi\mu d_p}. \tag{5.1}$$

In order to establish an initial condition that a finite number of particles are trapped in the inlet region of the pore, we use three successive steps separated by two air bubbles (figure 6(*a*)). The PDMS microfluidic channel is made by standard soft lithography and the channel block is bonded to a thin sheet of PDMS to ensure the same surface properties for all walls.

The pore is initially filled with a 10 mM NaCl solution. Then, the 10 mM NaCl solution with suspended polystyrene (PS) particles, separated by a first air bubble from the original solution, is introduced in the main channel (width, height, and length are, respectively, $w = 1.2$ mm, $h = 200$ μm, and $\ell = 5$ cm) at a mean flow speed $\langle u \rangle \approx 2.5$ mm/s (figure 6($a - i$)). Once the two solutions come in contact with each other, particles start to accumulate at the pore inlet by the slight penetration of streamlines (penetration depth $\approx w$) (Battat *et al.* 2019). One minute after the particle suspension flows in the main channel, a second air bubble is introduced, followed by a 1 mM NaCl solution (figure 6($a - ii$)). Once the 1 mM NaCl solution contacts the liquid in the pore, the main channel flow speed is reduced to $\langle u \rangle = 25$ μm/s. Fluorescent images are then recorded every 10 seconds using an inverted microscope (Leica DMI4000B; figure 6($a-iii$)). Typical experimental images are shown in figure 6(*b*) as a time sequence.

For the three values of d_p, we compare the experiments with the one-dimensional model with 3D dispersion (figure 7). Details of the model are given in §4.2. The particle zeta potential has a strong influence on the peak location of the colloid distribution, and the wall zeta potential has a strong influence on the dispersion of the colloid distribution. The dimensionless particle zeta potential Ψ_p and wall zeta potential Ψ_w were calculated as fitting parameters for each experiment. The fitted parameters used in the simulations of each panel are: (*a*) $\Psi_p = -2.84,\ \Psi_w = -3.91$, (*b*) $\Psi_p = -3.31,\ \Psi_w = -3.26$, and (*c*) $\Psi_p = -3.04,\ \Psi_w = -2.06$. The zeta potentials are each calculated within $\Psi \pm 0.002$ using a least squares method that compares model and experiment.

Some variation in particle zeta potentials is expected due to the independent manufacturing of all three sizes of particles used. However, the variation in fitted wall zeta potentials is unexpected as pore walls properties were not changed between experiments.

It is possible that deviations from the predicted fluid velocity profile at the pore inlet, not captured by the Taylor dispersion model, enforce a bias of the particle size on the apparent dispersion of the colloid distribution (Battat *et al.* 2019). The sharp concentration gradient near the pore inlet at $\tau = 0$ causes a three to four order-of-magnitude decrease in the modified coefficient of diffusivity over the span of $\tau = 0 \to 0.05$ (figure 5(e)), meaning the the majority of the dispersion occurs near the inlet during this time-span. A small effect of particle size on the dispersion in this region can strongly impact the apparent dispersion of the colloid distribution throughout the pore. Therefore, it is not feasible with our current setup to accurately measure the wall zeta potential. In Appendix C, we perform an experiment holding particle size constant and calculate fitted potentials that demonstrate good agreement, supporting our claim that a particle-size dependence of the dispersion in the inlet region may be responsible for variations in the fitted values of the wall zeta potential.

The complex nature of the inlet region in microfluidic dead-end pores may also explain overestimation of the fitted particle zeta potentials. This effect is not due to imprecise measurements. In particular, in Appendix C we demonstrate precise fitting of zeta potentials for particles of the same batch. Full three-dimensional analysis including complex flow structure near the pore inlet may be helpful to further develop the dispersion system so that a direct mapping of the particle distribution versus the wall or particle potential values is possible for a wide range of surface properties. Additionally, it is possible that differences in manufacturing of each size of particle affected the diffusive behavior; a wide variation in particle zeta potential within a batch of one size could introduce an apparent spreading that contributes to the dispersion. Despite the imprecise fitted values of wall zeta potential, the very good agreement between the experimental data and the fitted simulation data supports our model.

6. Conclusions

We implemented a Taylor dispersion model of diffusiophoresis-driven particle motion in a dead-end pore. By integrating the effects of a 3D diffusioosmotic slip-driven flow into a 1D advective-diffusion equation, we performed direct comparisons between reduced-order simulations and experimental measurements. We also compared the effective dispersion model with direct numerical simulations, and obtained quantitative agreement for parameters up to the limit of applicability of the approximations typical of Taylor dispersion.

Our model builds upon previous studies of diffusiophoresis by including the effect of diffusioosmosis-driven dispersion. Furthermore, we extend previous analyses of Taylor dispersion by calculating the general form of a coefficient for a slip-driven flow with zero mean, accounting for spatial and temporal variations in the coefficient, and including the diffusiophoretic velocity in the reduced-order advective-diffusion equation.

Going forward, while our analysis focuses on the dead-end pore geometry with zero mean flow, it is straightforward to extend the analysis to other geometries and account for pressure and shear-driven flows (Chu *et al.* 2021). Similarly, while the results in this paper are for electrolytic diffusioosmosis, (3.18) can be utilized to calculate dispersion for non-electrolytic diffusioosmosis. Our analysis can also be combined with self-diffusiophoretic colloids that may have variance in mean velocities (Peng & Brady 2020). In summary, our dispersion model will enable rapid calculation of diffusioosmotic spreading for a wide variety of geometries, background flows, and physical processes.

An accurate calculation of dispersion in the presence of charged sidewalls can be exploited for various applications. For instance, lab-on-a-chip applications such as directed delivery of particles (Banerjee *et al.* 2016; Shi *et al.* 2016; Lee *et al.* 2018; Gandhi *et al.*

2020; Seo *et al.* 2020; Shin 2020) and zeta-potential measurement (Shin *et al.* 2017) rely on accurate prediction of particle concentration, which in turn is closely associated with colloidal dispersion. In physical systems such as energy storage and desalination devices (Biesheuvel & Bazant 2010; Florea *et al.* 2014; Gupta *et al.* 2020*a*,*c*; Bone *et al.* 2020; Henrique *et al.* 2022), it is common to observe ion concentration gradients inside charged pores, where one can expect colloidal transport and dispersion to be important. Finally, biophysical systems such as blood cells, phospholipid vesicles (Bruno *et al.* 2018; Hartman *et al.* 2018), plasmodesmata (Peters *et al.* 2021), and cell growth in microfluidic setups (Yang *et al.* 2018) also consist of charged surfaces, where diffusioosmosis plays a crucial role.

Acknowledgements. We thank the High Meadows Environmental Institute at Princeton University for partial support of this research and for supporting a summer internship for BMA. HAS thanks the NSF for support via grant CBET-2127563.

Declaration of Interest. The authors report no conflict of interest.

Appendix A. Deriving the coefficient of dispersion for a two-dimensional and a three-dimensional channel

The Taylor dispersion model introduced above, which we have generalized to account for streamwise and temporal variations in the dispersion coefficient for a channel geometry, a zero average fluid velocity, and a background 1D diffusiophoretic velocity field, is shown in this appendix to produce identical coefficients of dispersion as calculated many times previously for laminar flow between parallel plates in two dimensions and a rectangular conduit in three dimensions (Chatwin & Sullivan 1982). In this appendix we give a detailed calculation of the dispersion coefficients for slip-driven flow in narrow pores in two and three dimensions, depicted by figure 2.

Two-dimensional pore

Here we calculate the modified diffusion coefficient in slip-driven viscous flow for colloidal particles in a 2D dead-end pore of length ℓ and height $h \ll \ell$, where x spans $0 \to \ell$ and z spans $0 \to h$. The definition of the cross-sectional average from (3.4) becomes:

$$\langle f \rangle \equiv \frac{1}{h} \int_0^h f \, \mathrm{d}z, \tag{A 1}$$

and (3.10) reduces to:

$$v_{\mathrm{f}x} \frac{\partial \langle N \rangle}{\partial x} = D_{\mathrm{p}} \frac{\partial^2 N'}{\partial z^2}, \tag{A 2}$$

where the $x-$direction fluid velocity is (Alessio *et al.* 2021):

$$v_{\mathrm{f}x} = v_{\mathrm{s}} \left(1 - 6 \frac{z(h-z)}{h^2} \right). \tag{A 3}$$

Equation (3.11*c*) becomes:

$$\frac{\partial^2 f_{N'}}{\partial z^2} = -f_x = 6 \frac{z(h-z)}{h^2} - 1, \tag{A 4}$$

where $f_x = v_{\mathrm{f}x}/v_{\mathrm{s}}$. We integrate (A 4), apply the no-flux condition $\partial f_{N'}/\partial z(z = 0,\ h) = 0$, and require that $\langle f_{N'} \rangle = 0$ to obtain:

$$f_{N'} = \frac{z^4}{2h^2} - \frac{z^3}{h} + \frac{z^2}{2} - \frac{h^2}{60}, \tag{A 5}$$

from which we calculate:

$$\langle f_x f_{N'} \rangle = \frac{h^2}{210}. \tag{A 6}$$

We note that this is the standard coefficient for a channel flow with dispersion proportional to the square of the mean velocity.

Three-dimensional pore

We now consider a 3D pore, by introducing the width $w \ll \ell$, where y spans $0 \to w$ and $h < w$. In this case, the definition of the cross-sectional average from (3.4) becomes:

$$\langle f \rangle \equiv \frac{1}{wh} \int_0^w \int_0^h f \ \mathrm{d}z\mathrm{d}y, \tag{A 7}$$

and (3.10) becomes:

$$v_{\mathrm{f}x} \frac{\partial \langle N \rangle}{\partial x} = D_{\mathrm{p}} \left(\frac{\partial^2}{\partial y^2} + \frac{\partial^2}{\partial z^2} \right) N', \tag{A 8}$$

where the $x-$direction fluid velocity is, defining $y' \equiv y - w/2$:

$$v_{\mathrm{f}x} = v_{\mathrm{s}} \left(1 - 6\tilde{V} \left(\frac{z(h-z)}{h^2} - \frac{8}{\pi^3} \sum_{\substack{n \ \mathrm{odd} \\ \geqslant 1}}^{\infty} \frac{\cosh\left(n\pi \frac{y'}{h}\right) \sin\left(n\pi \frac{z}{h}\right)}{n^3 \cosh\left(\frac{1}{2} n\pi \frac{w}{h}\right)} \right) \right), \tag{A 9a}$$

$$\tilde{V} \equiv \left(1 - \frac{192}{\pi^5} \frac{h}{w} \sum_{\substack{n \ \mathrm{odd} \\ \geqslant 1}}^{\infty} \frac{\tanh\left(\frac{1}{2} n\pi \frac{w}{h}\right)}{n^5} \right)^{-1}. \tag{A 9b}$$

We note that the form of the fluid velocity in a channel is well-known for the case of pressure-driven flow, and for our case of slip-driven flow, the form of the velocity is identical upon transforming from the frame of the mean flow speed to the frame of the slip velocity (Alessio *et al.* 2021).

Equation (3.11*c*) becomes:

$$\left(\frac{\partial^2}{\partial y^2} + \frac{\partial^2}{\partial z^2} \right) f_{N'} = -f_x, \tag{A 10}$$

where $f_x = v_{\mathrm{f}x}/v_{\mathrm{s}}$. Following the example of Chatwin & Sullivan (1982), we represent the velocity in the convenient double cosine form, noting that in our case the cross-sectional average of the velocity is zero:

$$f_x = \sum_{\substack{p \ \mathrm{even} \\ \geqslant 2}}^{\infty} \alpha_{p0} \cos\left(p\pi \frac{y}{w}\right) + \sum_{\substack{q \ \mathrm{even} \\ \geqslant 2}}^{\infty} \alpha_{0q} \cos\left(q\pi \frac{z}{h}\right) + \sum_{\substack{p \ \mathrm{even} \\ \geqslant 2}}^{\infty} \sum_{\substack{q \ \mathrm{even} \\ \geqslant 2}}^{\infty} \alpha_{pq} \cos\left(p\pi \frac{y}{w}\right) \cos\left(q\pi \frac{z}{h}\right). \tag{A 11}$$

The coefficients are calculated from (A 9) using the Fourier method:

$$\alpha_{p0} = \frac{384wh\tilde{V}}{\pi^5} \sum_{\substack{n \text{ odd} \\ \geqslant 1}}^{\infty} \frac{\tanh\left(\frac{1}{2}n\pi\frac{w}{h}\right)}{n^3\left(n^2w^2 + p^2h^2\right)}, \tag{A 12a}$$

$$\alpha_{0q} = -\frac{24\tilde{V}}{q^2\pi^2}\left(1 + \frac{8}{\pi^2}\sum_{\substack{n \text{ odd} \\ \geqslant 1}}^{\infty} \frac{q^2}{n^2\left(n^2 - q^2\right)} \frac{\tanh\left(\frac{1}{2}n\pi\frac{w}{h}\right)}{\frac{1}{2}n\pi\frac{w}{h}}\right), \tag{A 12b}$$

$$\alpha_{pq} = -\frac{768wh\tilde{V}}{\pi^5} \sum_{\substack{n \text{ odd} \\ \geqslant 1}}^{\infty} \frac{\tanh\left(\frac{1}{2}n\pi\frac{w}{h}\right)}{n\left(n^2 - q^2\right)\left(n^2w^2 + p^2h^2\right)}. \tag{A 12c}$$

We solve (A 10) with the boundary conditions $\frac{\partial f_{N'}}{\partial z}(z = 0,\ h) = \frac{\partial f_{N'}}{\partial y}(y = 0,\ w) = 0$ and the requirement that $\langle f_{N'}\rangle = 0$ to obtain:

$$\begin{aligned} f_{N'} = &\sum_{\substack{p \text{ even} \\ \geqslant 2}}^{\infty} \left(\frac{w}{p\pi}\right)^2 \alpha_{p0} \cos\left(p\pi\frac{y}{w}\right) + \sum_{\substack{q \text{ even} \\ \geqslant 2}}^{\infty} \left(\frac{h}{q\pi}\right)^2 \alpha_{0q} \cos\left(q\pi\frac{z}{h}\right) \\ &+ \sum_{\substack{p \text{ even} \\ \geqslant 2}}^{\infty} \sum_{\substack{q \text{ even} \\ \geqslant 2}}^{\infty} \left(\left(\frac{w}{p\pi}\right)^2 + \left(\frac{h}{q\pi}\right)^2\right) \alpha_{pq} \cos\left(p\pi\frac{y}{w}\right) \cos\left(q\pi\frac{z}{h}\right). \end{aligned} \tag{A 13}$$

Finally, we calculate:

$$\langle f_x f_{N'}\rangle = \left(\frac{12\tilde{V}h}{\pi^3}\right)^2 \left(2\sum_{\substack{p \text{ even} \\ \geqslant 2}}^{\infty} \beta_{p0}^2 + 2\sum_{\substack{q \text{ even} \\ \geqslant 2}}^{\infty} \beta_{0q}^2 + \sum_{\substack{p \text{ even} \\ \geqslant 2}}^{\infty} \sum_{\substack{q \text{ even} \\ \geqslant 2}}^{\infty} \beta_{pq}^2\right), \tag{A 14a}$$

$$\beta_{p0} = -\frac{16}{p\pi^3} \sum_{\substack{n \text{ odd} \\ \geqslant 1}}^{\infty} \frac{\tanh\left(\frac{1}{2}n\pi\frac{w}{h}\right)}{n^3\left(n^2 + p^2\left(\frac{h}{w}\right)^2\right)}, \tag{A 14b}$$

$$\beta_{0q} = -\frac{1}{q^3}\left(1 + \frac{8}{\pi^2}\sum_{\substack{n \text{ odd} \\ \geqslant 1}}^{\infty} \frac{q^2}{n^2\left(n^2 - q^2\right)} \frac{\tanh\left(\frac{1}{2}n\pi\frac{w}{h}\right)}{\frac{1}{2}n\pi\frac{w}{h}}\right), \tag{A 14c}$$

$$\beta_{pq} = -\frac{32}{\pi^3} \frac{h/w}{p^2\left(\frac{h}{w}\right)^2 + q^2} \sum_{\substack{n \text{ odd} \\ \geqslant 1}}^{\infty} \frac{\tanh\left(\frac{1}{2}n\pi\frac{w}{h}\right)}{n\left(n^2 - q^2\right)\left(n^2 + p^2\left(\frac{h}{w}\right)^2\right)}, \tag{A 14d}$$

where $\tilde{V}$ is defined by (A 9*b*).

Appendix B. Applicability of two- and three-dimensional velocity profiles in experimental analyses

As explained in the main text, dispersion of a particle patch cannot be fully described with a 2D model. Schematics of z-projection imaging are shown in figure 8. Compaction experiments typically show an exclusion boundary that indicates an influence of the z-averaged flow velocity inside a pore. This can be approximated by a 2D parabolic velocity (figure 9(*c*)). 3D dispersion of a particle patch requires understanding the 3D velocity

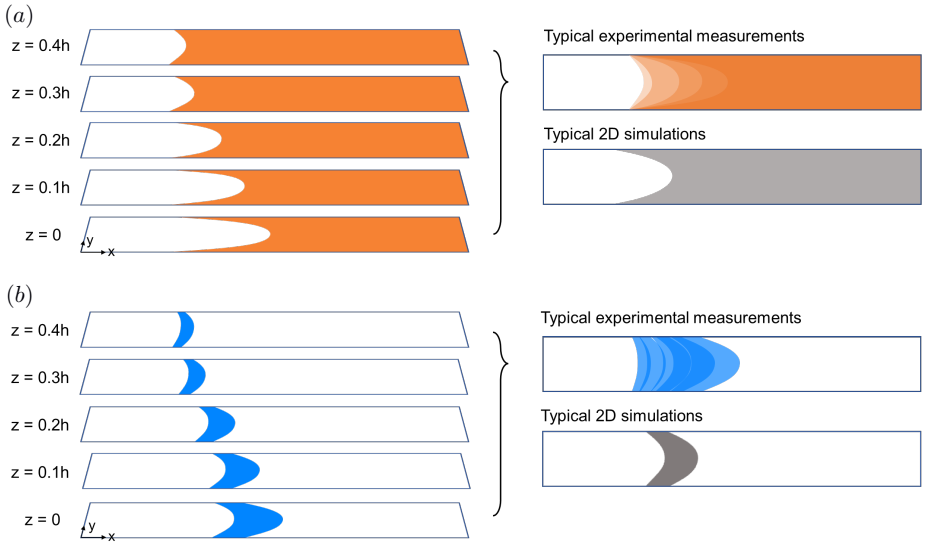

FIGURE 8. Schematics showing the difference between the compaction and dispersion experiments in terms of 2D imaging. (a) The z-projection of compaction experiments shows an apparent boundary that can be estimated with a flow velocity obtained for the 2D pore. (b) The z-projection of the dispersion experiments cannot be fully described by the 2D pore model.

distribution inside a dead-end pore (figure 8(b)), as the 2D projected particle distribution reveals 3D flow profiles.

In the current experiment, while the particle patch is moving toward the dead-end by 1D diffusiophoresis, each particle experiences different flow speeds at different locations inside the pore. If the initial particle distribution was uniform along the pore and diffusiophoretic compaction occurs, we obtain the particle exclusion boundary that is affected by the z-averaged flow velocity (figures 8(a) and 9(c)), due to the 2D projection nature of imaging. In contrast, when there is diffusiophoresis of a particle patch, the stretched particle distribution due to 3D flow in the pore is revealed in the z-projection images, as illustrated in figures 1(c), 8(b) and 9(a, b).

In the particle-patch experiments performed with short pores (figure 1), PS particles aligned with the flow velocity in the pores with different heights (figure 9(a, b)). Flow velocities at two different z locations ($z = 5$ μm from the wall and $z = h/2$) indicate that variation in the dispersion profiles in different pores is due to different flow speeds (figure 9(b)).

Appendix C. Experiments with variation of solute concentration

In order to investigate the particle-size dependence on the dispersion (§5), we performed an experiment holding particle size constant ($d_\mathrm{p} = 0.5$ μm). The solute concentration ratio $c_\mathrm{m}/c_\mathrm{p}$ was set to 0.05 to compare to the previous experiment with a ratio of 0.1, where c_m is the initial solute concentration in the main channel and c_p is the initial solute concentration in the pore.

In figure 11 we show the two experiments for (a) $c_\mathrm{m}/c_\mathrm{p} = 0.1$ and (b) $c_\mathrm{m}/c_\mathrm{p} = 0.05$ compared to simulations with fitted particle and wall zeta potentials, calculated to be: (a) $\Psi_\mathrm{p} = -3.31$, $\Psi_\mathrm{w} = -3.26$ and (b) $\Psi_\mathrm{p} = -3.46$, $\Psi_\mathrm{w} = -3.29$. The zeta potentials were fit with a least squares routine to $\Psi \pm 0.002$. The values of Ψ_w were consistent with

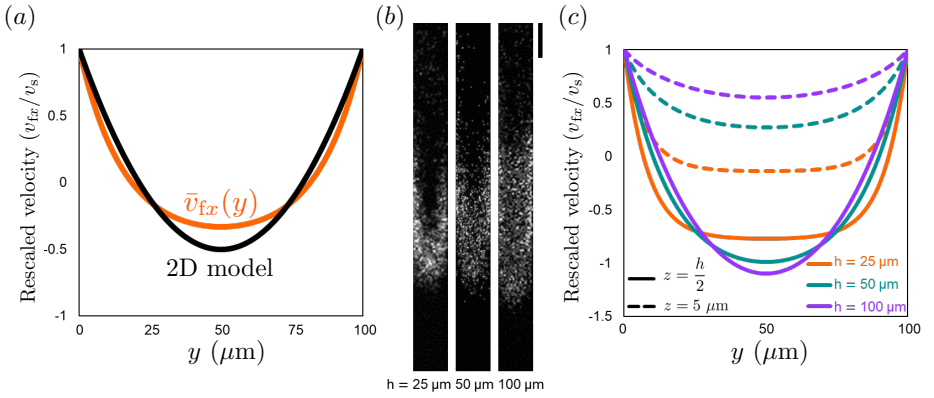

FIGURE 9. Qualitative interpretation of the particle dispersion in short pores (figure 1) by the differences in flow velocities. (a) Images obtained from the pores with $w = 100$ μm, $\ell = 1$ mm and three different heights ($h = 25,\ 50$, and 100 μm). (b) Flow velocities obtained from different pores plotted versus pore width. Two z-positions are selected: $z = 5$ μm (from the wall), and $z = h/2$ for all three pores, and difference in the flow velocities $v_f(x, y, h/2) - v_f(x, y, z = 5\ \mu\text{m})$ can qualitatively describe the variation in the particle distributions. (c) Comparison between the z-averaged flow velocity obtained from the 3D pore and the 2D parabolic flow velocities. The cross section of the 3D pore is $w = 100$ μm and $h = 50$ μm, and the 2D pore has the same width.

FIGURE 10. Figure 6(b) without intensity enhancement. Scale bar is 100 μm.

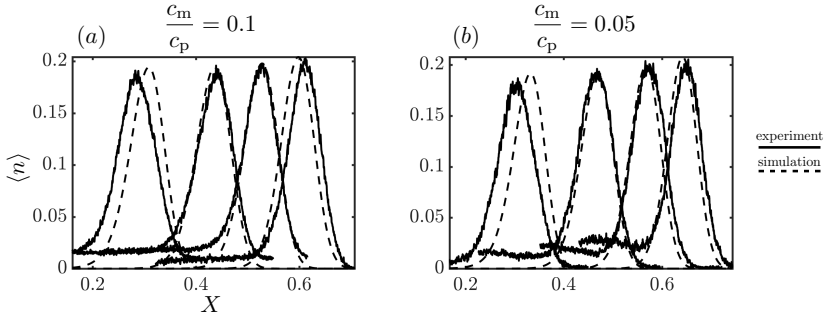

FIGURE 11. Comparison of experimental data (solid) to simulated data (dashed) for two different values of initial solute concentration ratio: (a) $c_m/c_p = 0.1$ and (b) $c_m/c_p = 0.05$. The distributions, in order of peak location from left to right, correspond to times $\tau = 0.1,\ 0.2,\ 0.3$, and 0.4. Fitting parameters are dimensionless particle zeta potential Ψ_p and wall zeta potential Ψ_w. The fitted zeta potentials were calculated to be: (a) $\Psi_p = -3.31$, $\Psi_w = -3.26$ and (b) $\Psi_p = -3.46$, $\Psi_w = -3.29$. Good agreement is found between (a) and (b).

an estimate we made using a different setup, where the particle entrainment front was tracked to measure the flow velocity (see figure 12). Independence of fitting parameters on the solute concentration ratio is expected; the particles are of the same batch so are expected to have the same zeta potential, and the possible particle-size effect on the dispersion is eliminated by holding particle size constant. The close agreement in the zeta

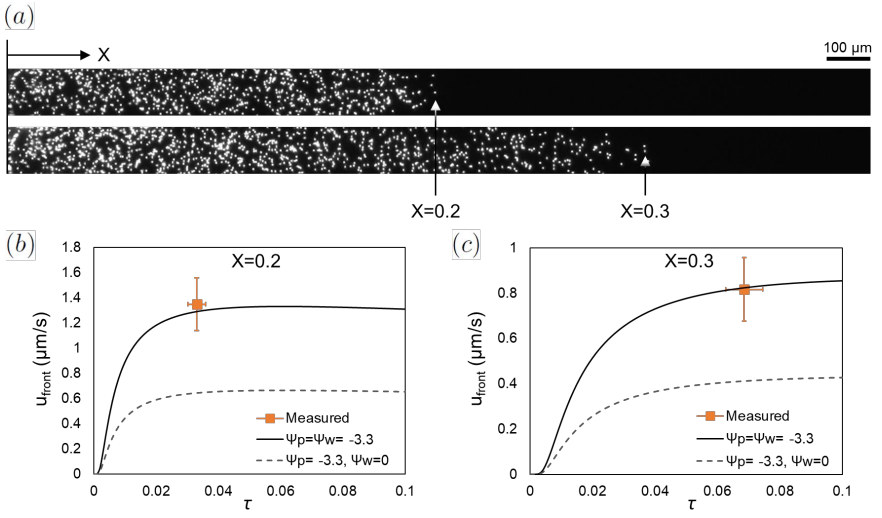

FIGURE 12. Independent estimation of wall zeta potential Ψ_w in our typical experimental setup. (a) Particle entrainment front was tracked at two separate locations ($X = 0.2,\ X = 0.3$), and the centerline velocity was compared with calculations. For the pores with $w/h = 2$, the particle speed along the centerline is $V_{DP} + |V_s|$. ($b-c$) A choice of the wall potential value $\Psi_w = -3.3$ is seen to reasonably agree with the measurements, supporting the consistency of our zeta potential fitting.

Particles	d_p (μm)	Measured ψ_p (mV)	Fitted ψ_p (mV)	Concentration (%v/v)
Polystyrene (Invitrogen)	1.0	-70.92 ± 2.23	-78.13	0.1
Carboxylate-modified polystyrene (Sigma Aldrich)	0.5	-75.13 ± 0.35	-85.07	0.2
Polystyrene (Bangs Laboratories)	0.2	-50.51 ± 1.02	-72.99	0.2

TABLE 1. Particles used in the experiments.

potentials of each experiment supports our model and the possibility of a particle-size effect on the dispersion near the pore inlet.

Appendix D. Particles used in the experiments

In the experiments, three different particles are used to visualize diffusiophoresis and dispersion in the dead-end pores. Particle information is listed in Table 1.

REFERENCES

ABÉCASSIS, B., COTTIN-BIZONNE, C., YBERT, C., AJDARI, A. & BOCQUET, L. 2008 Boosting migration of large particles by solute contrasts. *Nature Materials* **7** (10), 785–789.

ABÉCASSIS, B., COTTIN-BIZONNE, C., YBERT, C., AJDARI, A. & BOCQUET, L. 2009 Osmotic manipulation of particles for microfluidic applications. *New Journal of Physics* **11** (7), 075022.

AHMED, T. & STOCKER, R. 2008 Experimental verification of the behavioral foundation of bacterial transport parameters using microfluidics. *Biophysical Journal* **95**, 4481–4493.

ALESSIO, B.M., SHIM, S., MINTAH, E., GUPTA, A. & STONE, H.A. 2021 Diffusiophoresis and

diffusioosmosis in tandem: Two-dimensional particle motion in the presence of multiple electrolytes. *Physical Review Fluids* **6** (5), 054201.

Aminian, M., Bernardi, F., Camassa, R., Harris, D.M. & McLaughlin, R.M. 2016 How boundaries shape chemical delivery in microfluidics. *Science* **354** (6317), 1252–1256.

Aris, R. 1956 On the dispersion of a solute in a fluid flowing through a tube. *Proceedings of the Royal Society of London. Series A. Mathematical and Physical Sciences* **235** (1200), 67–77.

Ault, J.T., Shin, S. & Stone, H.A. 2019 Characterization of surface-solute interactions by diffusioosmosis. *Soft Matter* **15**, 1582–1596.

Ault, J.T., Warren, P.B., Shin, S. & Stone, H.A. 2017 Diffusiophoresis in one-dimensional solute gradients. *Soft Matter* **13** (47), 9015–9023.

Banerjee, A., Williams, I., Azevedo, R.N., Helgeson, M.E. & Squires, T.M. 2016 Soluto-inertial phenomena: Designing long-range, long-lasting, surface-specific interactions in suspensions. *Proceedings of the National Academy of Sciences* **113** (31), 8612–8617.

Battat, S., Ault, J.T., Shin, S., Khodaparast, S. & Stone, H.A. 2019 Particle entrainment in dead-end pores by diffusiophoresis. *Soft Matter* **15** (19), 3879–3885.

Biesheuvel, P.M. & Bazant, M.Z. 2010 Nonlinear dynamics of capacitive charging and desalination by porous electrodes. *Physical Review E* **81** (3), 031502.

Bone, S.E., Steinrück, H. & Toney, M.F. 2020 Advanced characterization in clean water technologies. *Joule* **4** (8), 1637–1659.

Bruno, G., Di Trani, N., Hood, R.L., Zabre, E., Filgueira, C.S., Canavese, G., Jain, P., Smith, Z., Demarchi, D., Hosali, S. & others 2018 Unexpected behaviors in molecular transport through size-controlled nanochannels down to the ultra-nanoscale. *Nature Communications* **9** (1), 1–10.

Chatwin, P.C. & Sullivan, P.J. 1982 The effect of aspect ratio on longitudinal diffusivity in rectangular channels. *Journal of Fluid Mechanics* **120**, 347–358.

Chu, H.C.W., Garoff, S., Tilton, R.D. & Khair, A.S. 2020 Advective-diffusive spreading of diffusiophoretic colloids under transient solute gradients. *Soft Matter* **16** (1), 238–246.

Chu, H.C.W., Garoff, S., Tilton, R.D. & Khair, A.S. 2021 Macrotransport theory for diffusiophoretic colloids and chemotactic microorganisms. *Journal of Fluid Mechanics* **917**.

Derjaguin, B.V., Sidorenkov, G.P., Zubashchenkov, E.A. & Kiseleva, E.V. 1947 Kinetic phenomena in boundary films of liquids. *Kolloidn. zh* **9** (01).

Doshi, M.R., Daiya, P.M. & Gill, W.N. 1978 Three dimensional laminar dispersion in open and closed rectangular conduits. *Chemical Engineering Science* **33** (7), 795–804.

Florea, D., Musa, S., Huyghe, J.M.R. & Wyss, H.M. 2014 Long-range repulsion of colloids driven by ion exchange and diffusiophoresis. *Proceedings of the National Academy of Sciences* **111** (18), 6554–6559.

Gandhi, T., Mac Huang, J., Aubret, A., Li, Y., Ramananarivo, S., Vergassola, M. & Palacci, J. 2020 Decision-making at a t-junction by gradient-sensing microscopic agents. *Physical Review Fluids* **5** (10), 104202.

Gupta, A., Rajan, A.G., Carter, E.A. & Stone, H.A. 2020*a* Ionic layering and overcharging in electrical double layers in a poisson-boltzmann model. *Physical Review Letters* **125** (18), 188004.

Gupta, A., Shim, S. & Stone, H.A. 2020*b* Diffusiophoresis: from dilute to concentrated electrolytes. *Soft Matter* **16** (30), 6975–6984.

Gupta, A., Zuk, P.J. & Stone, H.A. 2020*c* Charging dynamics of overlapping double layers in a cylindrical nanopore. *Physical Review Letters* **125** (7), 076001.

Hartman, S.V., Božič, B. & Derganc, J. 2018 Migration of blood cells and phospholipid vesicles induced by concentration gradients in microcavities. *New Biotechnology* **47**, 60–66.

Henrique, F., Zuk, P.J. & Gupta, A. 2022 Charging dynamics of electrical double layers inside a cylindrical pore: predicting the effects of arbitrary pore size. *Soft Matter* .

Kar, A., Chiang, T., Ortiz Rivera, I., Sen, A. & Velegol, D. 2015 Enhanced transport into and out of dead-end pores. *ACS Nano* **9** (1), 746–753.

Keh, H.J. & Ma, H.C. 2005 Diffusioosmosis of electrolyte solutions along a charged plane wall. *Langmuir* **21** (12), 5461–5467.

Lee, H., Kim, J., Yang, J., Seo, S.W. & Kim, S.J. 2018 Diffusiophoretic exclusion of colloidal particles for continuous water purification. *Lab on a Chip* **18** (12), 1713–1724.

McDermott, J.J., Kar, A., Daher, M., Klara, S., Wang, G., Sen, A. & Velegol, D. 2012 Self-generated diffusioosmotic flows from calcium carbonate micropumps. *Langmuir* **28** (44), 15491–15497.

Migacz, Robben E & Ault, Jesse T 2022 Diffusiophoresis in a taylor-dispersing solute. *Physical Review Fluids* **7** (3), 034202.

Nery-Azevedo, R., Banerjee, A. & Squires, T.M. 2017 Diffusiophoresis in ionic surfactant gradients. *Langmuir* **33** (38), 9694–9702.

Palacci, J., Abécassis, B., Cottin-Bizonne, C., Ybert, C. & Bocquet, L. 2010 Colloidal motility and pattern formation under rectified diffusiophoresis. *Physical Review Letters* **104** (13), 138302.

Palacci, J., Cottin-Bizonne, C., Ybert, C. & Bocquet, L. 2012 Osmotic traps for colloids and macromolecules based on logarithmic sensing in salt taxis. *Soft Matter* **8** (4), 980–994.

Paustian, J.S., Angulo, C.D., Nery-Azevedo, R., Shi, N., Abdel-Fattah, A.I. & Squires, T.M. 2015 Direct measurements of colloidal solvophoresis under imposed solvent and solute gradients. *Langmuir* **31** (15), 4402–4410.

Peng, Z. & Brady, J.F. 2020 Upstream swimming and Taylor dispersion of active brownian particles. *Physical Review Fluids* **5** (7), 073102.

Peters, W.S., Jensen, K.H., Stone, H.A. & Knoblauch, M. 2021 Plasmodesmata and the problems with size: interpreting the confusion. *Journal of Plant Physiology* **257**, 153341.

Prieve, D.C., Anderson, J.L., Ebel, J.P. & Lowell, M.E. 1984 Motion of a particle generated by chemical gradients. part 2. electrolytes. *Journal of Fluid Mechanics* **148**, 247–269.

Rasmussen, M.K., Pedersen, J.N. & Marie, R. 2020 Size and surface charge characterization of nanoparticles with a salt gradient. *Nature Communications* **11** (1), 1–8.

Raynal, F. & Volk, R. 2019 Diffusiophoresis, batchelor scale and effective péclet numbers. *Journal of Fluid Mechanics* **876**, 818–829.

Seo, M., Park, S., Lee, D., Lee, H. & Kim, S.J. 2020 Continuous and spontaneous nanoparticle separation by diffusiophoresis. *Lab on a Chip* **20**, 4118–4127.

Shi, N., Nery-Azevedo, R., Abdel-Fattah, A.I. & Squires, T.M. 2016 Diffusiophoretic focusing of suspended colloids. *Physical Review Letters* **117** (25), 258001.

Shimokusu, T.J., Maybruck, V.G., Ault, J.T. & Shin, S. 2019 Colloid separation by CO2-induced diffusiophoresis. *Langmuir* **36** (25), 7032–7038.

Shin, S. 2020 Diffusiophoretic separation of colloids in microfluidic flows. *Physics of Fluids* **32** (10), 101302.

Shin, S., Ault, J.T., Feng, J., Warren, P.B. & Stone, H.A. 2017 Low-cost zeta potentiometry using solute gradients. *Advanced Materials* **29** (30), 1701516.

Shin, S., Um, E., Sabass, B., Ault, J.T., Rahimi, M., Warren, P.B. & Stone, H.A. 2016 Size-dependent control of colloid transport via solute gradients in dead-end channels. *Proceedings of the National Academy of Sciences* **113** (2), 257–261.

Singh, N., Vladisavljević, G.T., Nadal, F., Cottin-Bizonne, C., Pirat, C. & Bolognesi, G. 2020 Reversible trapping of colloids in microgrooved channels via steady-state solute gradients. *Physical Review Letters* **125** (24), 248002.

Stone, H.A. & Brenner, H. 1999 Dispersion in flows with streamwise variations of mean velocity: radial flow. *Industrial & Engineering Chemistry Research* **38** (3), 851–854.

Taylor, G.I. 1953 Dispersion of soluble matter in solvent flowing slowly through a tube. *Proceedings of the Royal Society of London. Series A. Mathematical and Physical Sciences* **219** (1137), 186–203.

Velegol, D., Garg, A., Guha, R., Kar, A. & Kumar, M. 2016 Origins of concentration gradients for diffusiophoresis. *Soft Matter* **12** (21), 4686–4703.

Williams, I., Lee, S., Apriceno, A., Sear, R.P. & Battaglia, G. 2020 Diffusioosmotic and convective flows induced by a nonelectrolyte concentration gradient. *Proceedings of the National Academy of Sciences* **117** (41), 25263–25271.

Wilson, J.L., Shim, S., Yu, Y.E., Gupta, A. & Stone, H.A. 2020 Diffusiophoresis in multivalent electrolytes. *Langmuir* .

Yang, D., Jennings, A.D., Borrego, E., Retterer, S.T. & Männik, J. 2018 Analysis

of factors limiting bacterial growth in pdms mother machine devices. *Frontiers in Microbiology* **9**.